Received: 13 September 2018 | Revised: 22 February 2019 | Accepted: 24 March 2019

DOI: 10.1002/stc.2363

RESEARCH ARTICLE

WILEY

Displacement/velocity-based control of a liquid spring—MR damper for vertical isolation

Walaa Eltahawy[1] | Keri Ryan[1] | Sevki Cesmeci[2] | Faramarz Gordaninejad[2]

[1] Department of Civil and Environmental Engineering, University of Nevada, Reno, Reno, Nevada

[2] Department of Mechanical Engineering, Georgia Southern University, Statesboro, Georgia

Correspondence
Walaa Eltahawy, Department of Civil and Environmental Engineering, University of Nevada, Reno, Reno, NV.
Email: walaaeltahawy@nevada.unr.edu

Funding information
National Science Foundation, Grant/Award Number: CMMI 1437003

Summary

Seismic isolation is an effective technique used to mitigate effects of shaking and helps to achieve higher seismic performance. Recent researches have suggested that vertical excitation has significant effects on structures behavior during earthquake. In this study, three-dimensional (3D) isolation is proposed that combines an elastomeric bearing to resist horizontal ground shaking in series with a bilinear liquid spring (BLS)–controllable magnetorheological fluid damper (CMRD) to resist vertical shaking. A numerical model of a simplified rigid 2D block was developed to predict BLS-CMRD response under earthquake loading. The response of the BLS-CMRDs was simulated through a combination of nonlinear stiffness and viscous and hysteretic (semi-active) damping. A Disp/Vel-based control strategy was proposed that adjusts the input current according to the instantaneous vector combination of feedback displacement and velocity of the damper. Two variations of the control strategy were explored. First, with linear current variation, the current is activated when a threshold lower bound vector magnitude is reached, and maximum current is applied when threshold upper bound magnitude is exceeded. Second, the simplified ON–OFF strategy uses single threshold vector magnitude that triggers the maximum current to turn on when the instantaneous vector magnitude exceeds the threshold, and turn off otherwise. Results show that for ground motions that exceed the design level, Disp/Vel-based Control is effective to moderate the level of energy dissipation, keep the device vertical displacement within the design stroke limit, and attenuate vertical acceleration below PGA. In addition, Disp/Vel-based control reduces all responses relative to the well-known clipped optimal strategy used for structural control.

KEYWORDS

liquid spring, magnetorheological damper, seismic isolation, vertical acceleration, vertical isolation

1 | INTRODUCTION

Seismic isolation systems for buildings are designed to minimize structural and nonstructural damage during and after an earthquake event. However, recent studies have suggested that vertical excitation has significant effects on the behavior of building structures during earthquakes, especially on nonstructural elements. Furukawa et al.[1] conducted a full-scale shaking test of a four-story base-isolated reinforced concrete building. The test showed that vertical accelerations were

https://doi.org/10.1002/stc.2363

significantly amplified relative to the ground in some cases in a building with rubber isolation bearings, and vertical accelerations of up to 4 g were recorded in the floor slabs. This level of vertical shaking led to substantial disruption to unanchored medical equipment. Another full-scale shaking test of a five-story base-isolated steel moment frame building was carried out by Ryan et al.[2] In this study, vertical accelerations at column locations were amplified relative to the shake table by factors generally less than 2, whereas accelerations at mid-slab were amplified by average factors of approximately 3 on the second floor up to 6 on the roof. Peak vertical accelerations in excess of 8 g were recorded in floor slabs. Observed nonstructural and content damage was attributed to large vertical input acceleration, because the horizontal floor accelerations were constrained to relatively low levels. Damage to the suspended ceiling and piping system was evaluated systematically for each shaking simulation.[2] Damage was found to be minimal for accelerations from 2 to 3 g, moderate for accelerations from 3 to 5 g, and extensive for accelerations exceeding 5 g. Both tests clarified that nonstructural component and content responses are greatly affected by vertical excitation intensity.

In the past, researchers have proposed to combine both horizontal and vertical isolation in series or develop three-dimensional (3D) isolation devices to achieve better performance.[3] For example, Suhara et al.[4,5] developed and tested 3D isolation by combining laminated rubber bearings as horizontal isolators in series with rolling seal type air springs as vertical isolators. The rolling seal type air spring is a steel/concrete cylinder lowered into an air cavity and attached with a rolling rubber seal. Kashiwazaki et al.[6] developed and tested a hydraulic system consisting of load-carrying hydraulic cylinders filled with nitrogen gas for vertical isolation, also connected in series with laminated rubber bearings. Kageyama et al.[7,8] proposed a 3D isolation system consisting of cable reinforced air springs. The 3D air spring was composed of an inner cylinder attached to the base and an outer cylinder attached to the structure separated by an air cavity bounded by a flexible rubber sheet.

The proposed systems have vertical isolation periods on the order of 1–2 s and generally utilize dampers and rocking suppression devices to control both vertical and rocking displacements. Zhou et al.[9] examined the dynamic performance of several vertical and 3D isolation systems for potential application to modern nuclear facilities. An isolation system with vertical period $T_z = 0.33$ s was found to be feasible for the nuclear power plant model examined and could effectively reduce the vertical in-structure responses. Also, Zhou concluded that the rocking effect was obvious when T_z increased to 1.0 s, and the vertical isolator displacements were at least as large as the horizontal displacements for $T_z = 2.3$ s. In addition, the authors explored the fundamental dynamic response of structures with 3D isolation systems using a simplified model of a rigid block resting on isolation bearings.[10] A parametric study was carried out to evaluate the effect of different site conditions, structure properties, and 3D isolation parameters on the structure and isolator responses. The results showed that an acceptable range for the vertical isolation period is $T_z = 0.5$–1.0 s, provided that the horizontal isolation period T_x is around three to four times greater than T_z and sufficient damping (equivalent viscous damping of 20%) is provided in both directions.

Utilizing this insight on the effective design of a 3D isolation system, Cesmeci et al.[11] developed a new device for vertical isolation, a bilinear liquid-spring BLS–controllable magnetorheological fluid damper CMRD that can also transmit the shear in the transverse direction. The bilinear stiffness was devised to stiffen the device to arrest tension while simultaneously attenuating the vertical acceleration. The optimal parameters were found to be tension stiffness approximately four times the compression stiffness ($k_t \approx 4k_c$).[10] Recently, many researchers studied the capabilities of CMRDs and concluded that they have high potential for control of seismic-induced vibration.[12,13] In such semi-active devices, the MR damping is activated by an input current.[14-16] This controllable damping can be used to optimize energy dissipation according to earthquake intensity and limit the stroke of the BLS-CMRD to below its capacity.

Effective use of controllable damping helps the isolation system to accommodate a wider range of demands, and especially high intensity demands. Several semi-active control algorithms have been proposed, such as bang-bang, decentralized bang-bang, and clipped optimal.[17] Leitmann[18] applied Lyapunov's direct approach for the design of a semi-active controller. This algorithm is classified as a bang-bang controller and is dependent on the sign of the measured control force and the states of the system. These states are estimated based on available measurements (e.g., device displacement, device forces, and structural accelerations) using the Kalman filter. The effectiveness of the algorithm depends on balanced measurements of the responses throughout the full structure.[18] McClamroch and Gavin[19] also used Lyapunov's direct approach to develop the decentralized bang-bang control law. In this approach, the Lyapunov function was chosen to represent the total vibratory energy in the structure (kinetic plus potential energy), which requires only the floor velocities and applied forces to be measured. Dyke et al.[20] proposed the clipped optimal control approach and found it to be effective for use with MR dampers. Clipped optimal control uses a linear optimal controller that calculates a desired control force based on measured structural responses and the measured applied force.[21] Through a force feedback loop, commands direct the MR damper to generate approximately the desired optimal control force. The bang-bang, decentralized bang-bang, and clipped optimal control approaches were compared on a three-story structure with MR dampers.[17] All three control algorithms varied in effectiveness for reducing different response parameters, and trade-offs were observed. Compared with the other algorithms, bang-bang control achieved, on average, a balanced (but small) reduction of the peak displacement, interstory displacement, and acceleration. However, the largest reduction in the peak acceleration was achieved with the decentralized bang-bang approach whereas the largest reductions in the peak roof and interstory displacements were achieved with the clipped optimal control. These previous control strategies were all ON–OFF strategies, meaning at every instant either full current or no current was applied. Performance might be improved by using strategies that impose smooth variation to the control force through variable current input rather than abrupt changes.

The objective of this paper is to present and evaluate a new control strategy for the semi-active BLS-CMRD device when subjected to vertical ground shaking. The devices are implemented on a 2D rigid block model of the isolated structure, which focuses on the dynamics of 3D isolation without being influenced by structural flexibility. In this strategy, the input current, which increases the controllable damping force, is set proportional to a vector valued function of the feedback displacement and velocity. Two variations of the proposed control approach are evaluated against the clipped optimal control strategy. The control strategies are evaluated by examining the following responses: peak values of vertical displacement and acceleration of the left BLS-CMRD and overall drift ratio of the rigid block. In addition, the potential for the control strategy to minimize energy usage is evaluated by introducing two additional parameters: operation time and energy ratio (relative to Passive-ON) for the controller. This research was conducted alongside development and testing of a quarter scale BLS-CMRD device in the Large Scale Structures Laboratory at University of Nevada, Reno. Therefore, the design properties of the BLS-CMRD device, the numerical model developed to simulate its semi-active behavior, and the system model representing BLS-CMRDs acting in series with elastomeric bearings for 3D isolation are all presented.

2 | NUMERICAL MODELING

A simplified 2D rigid block is used in this study to model a hypothetical building structure. The discussion in this section is based on a full-scale prototype structure. This block is supported on isolation bearings at each base corner as shown in Figure 1. The isolation system is modeled as a combination of linear springs and dashpots to resist horizontal

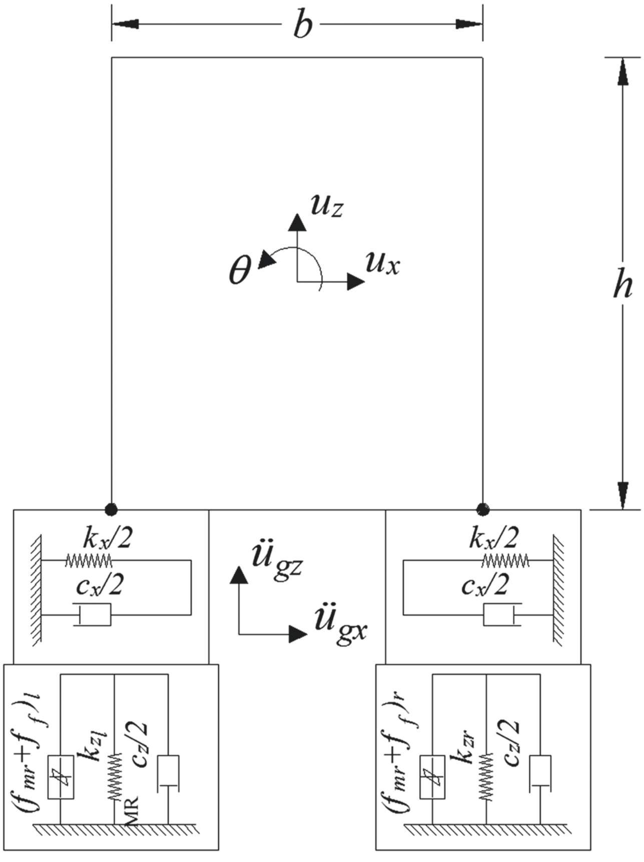

FIGURE 1 Rigid block used in the analysis

shaking in series with BLS-CMRDs to resist vertical shaking. The spring-dashpot is an adequate simplified representation of a traditional isolation device, such as an elastomeric bearing. Nonlinear springs are used to simulate BLS-CMRDs. The prototype block dimensions are height $h = 20$ m and width $b = 10$ m. This prototype block represents a hypothetical five-story building with dimensions similar to the test building used in the aforementioned NEES/E-Defense project.[2] This hypothetical building was assumed to be 20 m tall, 10 × 10 m and 2 bays × 2 bays in plan and resting on the stacked isolation devices. The block has mass m and moment of inertia i_θ lumped at the geometric center, which is also the center of mass CM. The model degrees-of-freedom (DOFs) are horizontal displacement u_x, vertical displacement u_z, and rotation θ of the block at its CM. The coupled equations of motion for the system subjected to horizontal and vertical ground accelerations $\ddot{u}_{gx}$ (t) and $\ddot{u}_{gz}$ (t) are the following:

$$\mathbf{M}\,\ddot{\mathbf{u}}+\mathbf{C}\,\dot{\mathbf{u}}+\mathbf{K}\,\mathbf{u}=-\mathbf{M}\,\ddot{\mathbf{u}}_{\mathrm{g}}-\mathbf{L}_{\mathrm{c}}\,\mathbf{f}_{\mathrm{c}} \tag{1}$$

or

$$\begin{bmatrix} m & 0 & 0 \\ 0 & m & 0 \\ 0 & 0 & i_\theta \end{bmatrix} \begin{Bmatrix} \ddot{u}_x\,(\mathrm{t}) \\ \ddot{u}_z\,(\mathrm{t}) \\ \ddot{\theta}\,(\mathrm{t}) \end{Bmatrix} + \begin{bmatrix} c_x & 0 & c_x{*}\frac{h}{2} \\ 0 & c_z & 0 \\ c_x{*}\frac{h}{2} & 0 & c_x{*}\frac{h^2}{4}+c_z{*}\frac{b^2}{4} \end{bmatrix} \begin{Bmatrix} \dot{u}_x\,(\mathrm{t}) \\ \dot{u}_z\,(\mathrm{t}) \\ \dot{\theta}\,(\mathrm{t}) \end{Bmatrix} + \begin{bmatrix} k_x & 0 & k_x{*}\frac{h}{2} \\ 0 & 0 & 0 \\ k_x{*}\frac{h}{2} & 0 & k_x{*}\frac{h^2}{4} \end{bmatrix} \begin{Bmatrix} u_x\,(\mathrm{t}) \\ u_z\,(\mathrm{t}) \\ \theta\,(\mathrm{t}) \end{Bmatrix}$$

$$= -\begin{bmatrix} m & 0 & 0 \\ 0 & m & 0 \\ 0 & 0 & i_\theta \end{bmatrix} \begin{Bmatrix} \ddot{u}_{\mathrm{gx}}\,(\mathrm{t}) \\ \ddot{u}_{\mathrm{gz}}\,(\mathrm{t}) \\ 0 \end{Bmatrix} - \begin{bmatrix} 0 & 0 & 0 & 0 \\ 1 & 0 & 1 & 0 \\ 0 & 1 & 0 & 1 \end{bmatrix} \begin{Bmatrix} k_{zr}u_{zr}+k_{zl}u_{zl} \\ (k_{zr}u_{zr}-u_{zl})^{*b}/_2 \\ \left(f_{mr}+f_f\right)_r+\left(f_{mr}+f_f\right)_l \\ \left(\left(f_{mr}+f_f\right)_r-\left(f_{mr}+f_f\right)_l\right)^{*b}/_2 \end{Bmatrix}, \tag{2}$$

where **M**, **C**, and **K** are mass, damping, and stiffness matrices of the system, respectively, $\mathbf{L}_c$ is the control force location matrix, and $\mathbf{f}_c$ is the control force vector that includes all nonlinear contributions to the equations of motion. The spring stiffness k_x and damping constant c_x represent the horizontal springs and dashpots, respectively, summed over all devices, and are defined consistent with assumed horizontal period $T_x = 3.0$ s and viscous damping ratio $\xi_{viscous,x} = 20\%$. Likewise, c_z is the vertical viscous damping constant used to compute viscous force $f_{viscous,z}$, summed over all BLS-CMRDs.

The control force vector, $\mathbf{f}_c$, includes terms with the following nonlinear contributions: vertical bilinear spring force $f_{spring,z}$ (expressed in terms of left and right isolator vertical stiffness k_{zl} and k_{zr}), the MR damping force f_{mr} that depends on the input current to the BLS-CMRD, and a friction force f_f generated from seal friction on the device. These nonlinear force contributions are explained in detail in Section 4. Both vertical spring and MR forces are calculated at each isolator and then transformed to the model DOFs. u_{zl} and u_{zr} are left and right isolator vertical displacement, which are calculated as u_z—$b/2{*}\theta$ and $u_z + b/2{*}\theta$, respectively. The developed numerical model was evaluated via a state-space approach to solve the coupled differential equations using Simulink's built-in solver.

3 | TARGET SPECTRA AND GROUND MOTION SCALING

Target spectra were developed to represent the seismic hazard in the horizontal and vertical direction, which determine the design stroke for BLS-CMRD. A hypothetical site location and soil type have been defined to obtain these target spectra. The hypothetical site is located in greater Los Angeles area on soil class D. This site has mapped risk-targeted maximum considered earthquake $\mathrm{MCE_R}$, 5% damped spectral acceleration of $S_s = 2.11$ g at short periods and $S_1 = 0.74$ g at 1.0-s period. The $\mathrm{MCE_R}$ horizontal and vertical target spectral accelerations have been calculated for this site according to ASCE 7-16[22] and FEMA-P750.[23] Equations to calculate these spectral accelerations are illustrated in Figure 2 for horizontal and vertical direction. In these equations, $S_{MS} = F_a\, S_S$ and $S_{M1} = F_v\, S_1$ where F_a and F_v are site coefficients for short periods and 1.0-s periods, respectively. For site class D and $S_s \geq 1.25$ g, $F_a = 1.0$, whereas $F_v = 1.5$ as $S_1 \geq 0.5$ g. According to Section 23 of FEMA-P750,[23] C_v is a vertical coefficient that depends on S_s and site class. From Figure 2, the

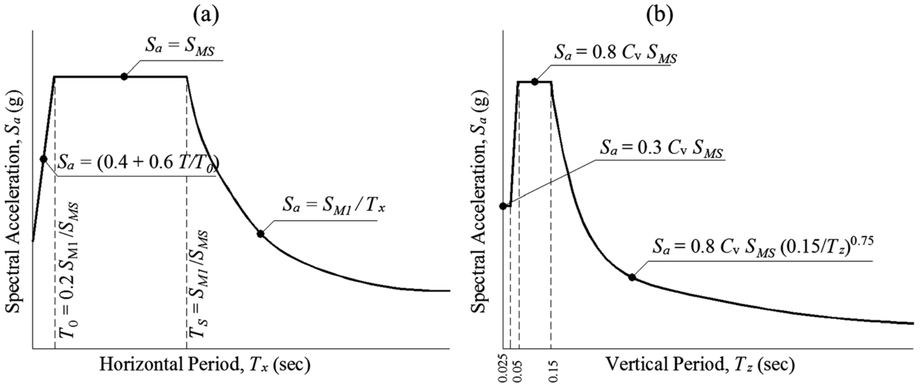

FIGURE 2 MCER spectrum (a) horizontal direction according to ASCE 7-16[22] and (b) vertical direction according to FEMA P-750[23]

peak vertical to horizontal spectral acceleration V/H ratio is observed to be 0.8 C_v. For site class D, C_v varies from 0.7 for $S_s \leq 0.2$ g to 1.5 for $S_s \geq 2.0$ g; consequently, the V/H ratio ranges from 0.56 to 1.2. Therefore, V/H = 1.2 for the selected site, which represents the largest intensity vertical hazard. The vertical spectral acceleration, adjusted for the effect of damping, is converted to a spectral displacement at the design natural period, which corresponds to the design stroke of the BLS-CMRD.

To study the effect of intense vertical shaking on the structural response, ground motions with relatively large vertical components were hand selected and scaled to represent the target spectra. These scaled ground motions are used in the numerical analysis conducted in this study to evaluate the proposed control approach. Initially, 30 recorded motions were selected from the PEER NGA database[24] by identifying ground motion triplets that by inspection best matched the shape and relative intensity of the components of the target spectra. These motions were amplitude-scaled to minimize the sum of the squared error between the response spectrum of the ground motion component and the target spectrum in each direction. The error was minimized over a period range from 1.5 to 4.0 s in both horizontal directions and from 0 to 2.0 s in the vertical direction. Both horizontal and vertical components were scaled by a single scale factor to preserve the relative component amplitudes of the original recorded motion, as referenced in the commentary of ASCE 7-16.[22]

These 30 motions were filtered to select a set of 12 motions to be used in the analysis. First, motions requiring a scale factor > 3.0 were removed to exclude ground motion distortion effects that may come from excessive scaling. Then, multiple attempts were made by trial and error to choose a smaller set of 12 motions with median spectra that matched the target spectra in two horizontal as well as vertical directions. Table 1 summarizes the selected ground motions and the calculated scale factors. The number of motions was limited because identifying motions that matched the target spectrum well in three directions using a single scale factor was found to be difficult. The medians of the 12 scaled ground motions are compared with $\mathrm{MCE_R}$ spectra for the horizontal x and vertical directions in Figure 3, as only one of the two horizontal components was used in this study. Due to inconsistencies between relative component amplitudes of recorded and target spectra, the median spectrum of the scaled ground motions falls short of the target spectrum in the vertical direction.

4 | DESIGN PROPERTIES OF BLS-CMRD FOR VERTICAL ISOLATION

This section describes the design and nonlinear model of the BLS-CMRD. Because this was in conjunction with experimental work, the model described from here onward represents the quarter scale BLS-CMRD fabricated and tested at UNR.[11] All analyses in this study were carried out for a one-quarter length scale model. Other basic scale factors based on appropriate similitude rules[25] are time scale factor = ½ and acceleration scale factor = 1:1. Applying these rules, the model block dimensions are $h = 5$ m and $b = 2.5$ m and the model horizontal spring stiffness corresponds to $T_x = 1.5$ s. Table 2 summaries the prototype and scaled model BLS-CMRD designed properties. The weight or dead load carried by a single BLS-CMRD was calculated based on the prototype block dimensions with devices distributed beneath the plan. The design stroke was computed based on selection of period, damping, and the developed $\mathrm{MCE_R}$ vertical target spectrum in the prototype domain and converted to the model domain using the similitude relations.

As introduced previously, the BLS-CMRD resists ground motion through the additive effects of f_{total} that combines spring force $f_{spring,z}$, viscous damping force $f_{viscous,z}$, friction force f_f and MR damping force f_{mr}. To achieve this

TABLE 1 Selected ground motions and scale factors

No.	Earthquake name	Year	Station name	Scale factor
1	Tabas, Iran	1978	Tabas	1.22
2	San Salvador	1986	Geotech Investig left	2.67
3	Loma Prieta	1989	LGPC	1.13
4	Manjil, Iran	1990	Abbar	1.81
5	Northridge	1994	LA–Sepulveda VA Hospital	2.16
6	Northridge	1994	Beverly Hills—14145 Mulhol	2.29
7	Northridge	1994	Jensen Filter Plant Generator Building	1.32
8	Chi-Chi, Taiwan	1999	TCU071	2.52
9	Chi-Chi, Taiwan	1999	TCU072	2.41
10	Chi-Chi, Taiwan	1999	TCU079	2.98
11	Chuetsu-oki	2007	Kashiwazaki NPP Unit 5: ground surface	1.65
12	L'Aquila, Italy	2009	L'Aquila–Parking	2.88

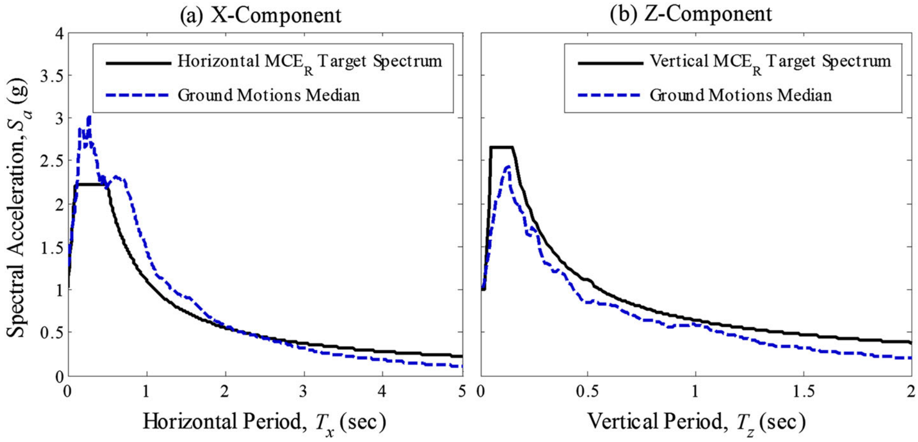

FIGURE 3 Median of 12 scaled ground motions compared with MCER spectra in (a) X-component and (b) Zcomponent

TABLE 2 Designed properties of prototype and model BLS-CMRD

Property	Prototype	Model
Period	0.5 s	0.25 s
Design stroke	±50 mm	±12.5 mm
Stroke limit (includes factor of safety and allowance for beyond MCE motions)	±100 mm	±25 mm
Weight for a single BLS-CMRD	1,484.8 kN	92.8 kN
Compression stiffness k_c	24,127.2 kN/m	6,031.8 kN/m
Tension stiffness k_t	102,684 kN/m	25,671 kN/m

resistance, the proposed BLS-CMRD consists of a cylinder that has two chambers separated by a sealing system, a shaft with a piston, two caps to close the two chambers, and four external rods to fasten the caps against the cylinder as shown in Figure 4. The top chamber is filled with MR fluid, whereas the bottom chamber is filled with pure silicone oil.[26]

For a single device with stiffness k_z, damping coefficient c_z, and subject to axial displacement u_z, the spring and viscous forces are calculated as follows:

$$f_{spring,z} = k_z u_z, \tag{3}$$

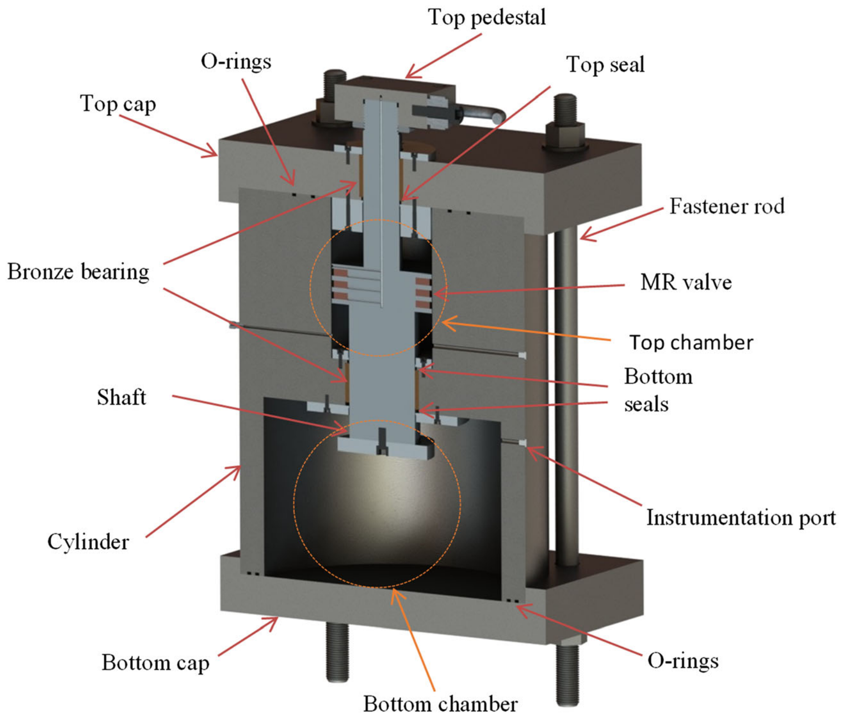

FIGURE 4 Cut-out view of the BLS-CMRD[26]

$$f_{viscous,z} = c_z \, \dot{u}_z = \left(1 + \frac{wh_g}{2a_p}\right) \frac{12\mu_{mr} l a_p{}^2}{wh_g{}^3} \, \dot{u}_z, \tag{4}$$

where h_g is the height of the flow gap (m), a_P is the effective piston area (m^2), μ_{mr} is the plastic viscosity of the MR fluid (kPa.sec), l is the effective axial pole length (m), and w is the piston width (m). Note that k_z takes on the value of k_t or k_c (Table 2) when the device is in compression (downward axial load) and tension (upward axial load), respectively. The friction between the seals and the shaft causes the friction force, f_{f} of approximately 5.5 kN (designed value) in the direction of motion. The MR force is activated by the input current i to the BLS-CMRD. The Bouc–Wen model[27] is used to calculate MR and friction force, which are combined into a single equation, expressed as follows:

$$f_{mr} + f_f = \alpha \frac{f_{\mathrm{y}}}{u_{\mathrm{y}}} u_{zr/l} + (1 - \alpha) f_y \delta, \tag{5}$$

$$u_{\mathrm{y}} \dot{\delta} = \left[a - \left(\beta \ \mathrm{sgn}\left(\dot{u}_{\frac{zr}{l}}\right) + \gamma\right) |z|^{\eta}\right], \tag{6}$$

where a, β, γ, and n are dimensionless quantities controlling the behavior of the model ($a = 1$, $\beta = .5$, $\gamma = .5$, and $\eta = 1$). In the Bouc–Wen model, $u_{\mathrm{y}} = 1$ mm is the yield displacement, $\alpha = .0001$ is the ratio of post-yield to pre-yield (elastic) stiffness, and δ is dimensionless hysteretic parameter that obeys a single nonlinear differential equation with zero initial condition. f_y is the yield force (kN) calculated as follows[27]:

$$f_y = \left(2.07 + \frac{12Q\mu_{mr}}{12Q\mu_{mr} + 0.4wh_g{}^2\tau_y}\right) \frac{\tau_y l a_p}{h_g} + 5.5, \tag{7}$$

$$\tau_y = 4.496 \ \tanh\left(1.108 \, i + 0.2893\right), \tag{8}$$

where Q is the flow rate through the annular gap (m^3/s) and τ_y is the dynamic yield stress (kPa) as calculated using Equation 8. The BLS-CMRD mechanics are explained and illustrated, and the design equations are derived in Cesmeci.[26]

Force displacement curves obtained from cyclic loading with amplitude ±25 mm, frequency 4 Hz, and current input $i = 1$ Amp are shown in Figure 5a. These values represent maximum allowed stroke, frequency corresponding to the vertical isolation period, and maximum applied current. The BLS-CMRD oscillates from the initial statically loaded state starting at the static displacement, $u_{static} = -15.47$ mm (compression). The contributions of viscous damping forces and MR damping forces—the latter of which includes friction—are shown separately and combined for the total effect. Viscous and MR damping forces depend on velocity, wherein the maximum velocity = 0.5 m/s is achieved at the initial/static displacement. The force-displacement curves for both viscous and MR damping are observed to be unsymmetric about the x-axis as the effective yield force is larger on the positive y-axis than the negative y-axis. This occurs because a_P for the rebound mode (piston moving toward the top chamber, Figure 4) is higher than that of the compression mode (piston moving toward the bottom chamber). This results in higher forces in the rebound (tension) mode for both viscous damping (Equation 4) and MR damping (Equation 7).[26] Maximum viscous damping forces are 31 and 72 kN, and maximum MR damping forces are 87 and 127 kN, in compression and tension, respectively.

Equivalent damping ratios (ξ) due to viscous and MR components are computed as follows:

$$\xi_{\text{viscous},z} = \frac{C_z}{C_{\text{cr}}}, \tag{9}$$

$$\xi_{\text{mr+f}} = \frac{1}{4\,\pi}\frac{E_{\text{d}}}{E_{\text{so}}}, \tag{10}$$

where c_{cr} = critical damping coefficient, E_{d} = energy dissipated in a cycle of harmonic vibration, and $E_{\text{so}} = 1/2 k_z {u_{zo}}^2$ is maximum strain energy. According to these equations, the device viscous damping is $\xi_{\text{viscous},z} = 20\%$, and equivalent viscous damping due to the MR component at the peak displacement of 25 mm is $\xi_{\text{mr + f}} = 40\%$. Because the viscous and equivalent viscous damping ratios depend on stiffness, $\xi_{\text{viscous},z}$ and $\xi_{\text{mr + f}}$ were calculated using the hysteresis loop obtained by applying the compression stiffness k_c for the cycle duration as shown in Figure 5b, because the compression stiffness is active during for the majority (about 80%) of the cycle.

5 | RESPONSE OF PASSIVELY DAMPED STRUCTURE

Passive-OFF and Passive-ON strategies are compared through response history analysis of the rigid block model subjected to the suite of 12 motions scaled to design level, to investigate the effect of full current-induced added damping on the overall structure behavior. During Passive-OFF, no current is applied in the analysis, whereas during Passive-ON, the maximum current of 1 Amp is applied continuously. Peak values of positive and negative vertical displacements (relative to the static displacement), vertical acceleration for the left BLS-CMRD, and overall drift ratio, are considered in this comparison. Peak responses differ at the left and right devices because of the rotation θ; however, the peak responses in the two devices were assumed to be similar when evaluated over many motions. The rigid block model drift ratio is computed as the ratio of relative horizontal displacement to the block height, which is shown to simplify to the

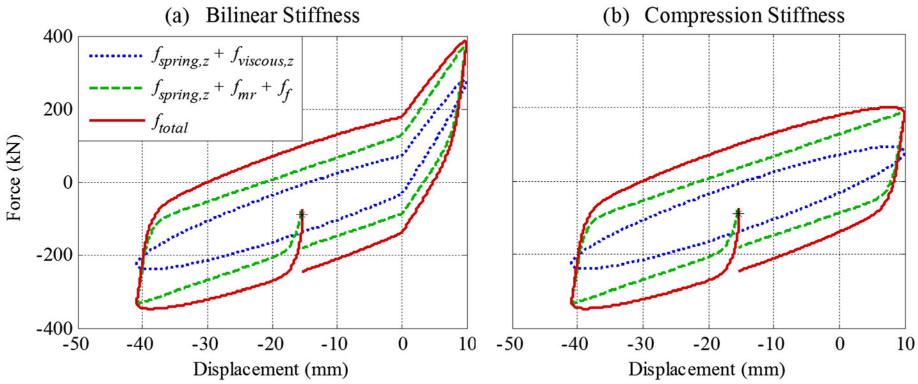

FIGURE 5 Force displacement curves obtained from cyclic loading with amplitude ±25 mm, frequency 4 Hz and current input 1 Amp; (a) true force-displacement with bilinear stiffness, (b) revised force-displacement with compression stiffness only to compute equivalent viscous damping

negative of the block rotation angle θ:

$$\text{Drift ratio} = \frac{\left(u_{x\ top} - u_{x\ bottom}\right)}{h} = \frac{\left(u_x - {}^{h}/_{2}\,\theta\right) - \left(u_x + {}^{h}/_{2}\,\theta\right)}{h} = -\theta. \tag{11}$$

In Equation (11), $u_{x\ top}$ is the horizontal displacement at the top of the rigid block and $u_{x\ bottom}$ is the horizontal displacement at the base or isolator level. The rigid block drift ratio (rotation angle) has been shown by the authors to be a good estimate of total roof drift in a flexible structure.[10] Also, because the BLS-CMRD vertical displacement depends on both u_Z and θ (Equation 2), the vertical displacement amplitude is naturally correlated with the drift ratio.

Left BLS-CMRD peak positive and negative vertical displacements, peak vertical acceleration, and overall drift ratio are presented in Figure 6. Peak responses are presented for each individual excitation; also shown are the median, 84th percentile, and 16th percentile over the suite of 12 motions. For n observed peak values y_i, the median (geometric mean) $\hat{y}$ and dispersion measure σ are defined as follows:

$$\hat{y} = \exp\left[\frac{\Sigma_{i=1}^{n} \ln y_i}{n}\right], \tag{12}$$

$$\sigma = \left[\frac{\Sigma_{i=1}^{n}\left(\ln y_i - \ln\hat{y}\right)^2}{n-1}\right]^{1/2}. \tag{13}$$

The 84th and 16th spercentiles are computed as $\hat{y}\exp(\sigma)$ and $\hat{y}/\exp(\sigma)$. These definitions assume that the data have been sampled from a lognormal distribution, which is found to be realistic of earthquake responses. The presented values illustrate both the expected response and the relative variation over a suite of motions. Peak relative positive and negative vertical displacements were calculated relative to $u_{static} = -15.47$ mm, and peak negative displacement is shown as a positive (absolute) value. A relative positive vertical displacement ≤ 15.47 mm means that no tension is sustained by the BLS-CMRD.

The median of peak BLS-CMRD displacements shows that with no added damping (Passive-OFF), the negative and positive vertical displacements remain below the design stroke (Table 2). Applying maximum current (Passive-ON case) reduces the vertical displacement at the isolator and the overall drift ratio but has the unwanted effect of increasing the BLS-CMRD vertical acceleration substantially, such that it exceeds the vertical PGA. However, a key objective of isolation is to attenuate the acceleration below PGA. This demonstrates a need for developing

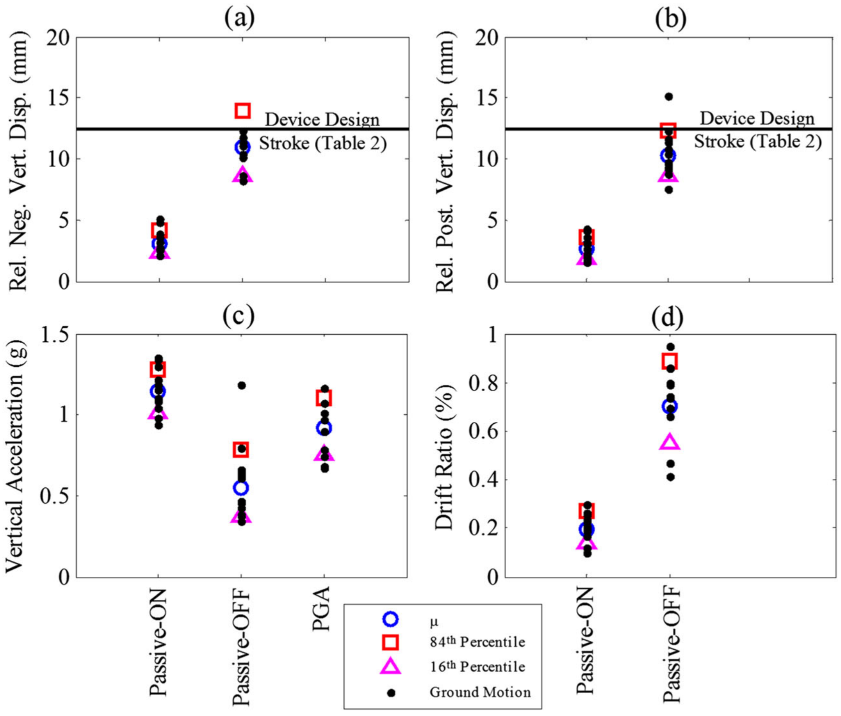

FIGURE 6 Peak responses at left BLS-CMRD, (a) relative negative vertical displacement, (b) relative positive vertical displacement, (c) vertical acceleration, (d) drift ratio

an effective control strategy to apply current in response to varying ground shaking intensity, with the objective of limiting the device displacement demands when necessary. Therefore, a control strategy is proposed that aims to simultaneously limit the vertical displacement to the device stroke capacity and attenuate vertical acceleration below PGA.

6 | DISPLACEMENT/VELOCITY (DISP/VEL)-BASED CONTROL

A control strategy is proposed that will adjust energy dissipation according to earthquake intensity and aims to limit the displacement or stroke of the BLS-CMRD below its capacity. In Disp/Vel-based control, the input current to the BLS-CMRD is calculated based on the combined feedback displacement and velocity of the damper. The need to control displacement is clear as the displacement demand drives the design of the device. However, waiting until high displacement is detected to activate MR damping may be only partially effective. Because velocity is the derivative of displacement and the two functions are out of phase for sinusoidal motion, high velocity will generally precede a large displacement excursion. Therefore, a control strategy that responds to both displacement and velocity may be better-equipped to optimize energy dissipation. Two variations of the strategy are proposed.

Strategy I. Linear current variation: In this control strategy, the state of the damper is modeled as a vector valued function $\mathbf{u_z} = <u_z, \dot{u}_z>^{\mathrm{T}}$, which are the vertical displacement and velocity, respectively. The input current is varied linearly with the instantaneous magnitude of the vector. The current is activated when a threshold lower bound vector magnitude is reached, and maximum current is applied when a threshold upper bound vector magnitude is reached. These threshold magnitudes are modeled as ellipse surfaces with displacement as the semi-major axis and velocity as the semi-minor axis; d_{min} and v_{min} are the magnitudes of displacement and velocity for the inner ellipse or MR activation surface, whereas d_{max} and v_{max} are magnitudes of displacement and velocity for the outer ellipse, denoted the MR capping surface. These ellipses are centered at u_{static} and represented by the following equations:

$$\left(\frac{u_z - u_{static}}{d_{min}}\right)^2 + \left(\frac{\dot{u}_z}{v_{min}}\right)^2 = 1 \qquad \text{(MR Activation Surface)}, \tag{14}$$

$$\left(\frac{u_z - u_{static}}{d_{max}}\right)^2 + \left(\frac{\dot{u}_z}{v_{max}}\right)^2 = 1 \qquad \text{(MR Capping Surface)}. \tag{15}$$

In this context, the ellipse semi-minor to semi-major axis ratio is interpreted as a peak displacement to velocity ratio d/v. The instantaneous applied current as a function of the feedback displacement u_z and velocity $\dot{u}_z$is calculated by the following equations:

$$\widehat{u} = \left(\frac{u_z - u_{static}}{d_{min}}\right)^2 + \left(\frac{\dot{u}_z}{v_{min}}\right)^2, \tag{16}$$

Case I: $\widehat{u} < 1 \quad \rightarrow \quad i = 0,$
Case II: $\widehat{u} \ > r^2 \quad \rightarrow \quad i = 1\ \text{amp},$
Case III: $1 < \widehat{u} < r^2 \quad \rightarrow \quad i = sx + i_{\text{o}},$

where r is the outer to the inner ellipse ratio ($r = d_{max}/d_{min} = v_{max}/v_{min}$). For Case III, the current varies linearly with x—the magnitude of the displacement and velocity vector—from the MR activation surface to the MR capping surface. The magnitude x, slope s and intercept i_{o} of the linear equation are given by the following:

$$x = \sqrt{\left(u_z - u_{static}\right)^2 + \left(\dot{u}_z {*}^{d}/_{v}\right)^2}, \tag{17}$$

$$s = \frac{1}{d_{max} - d_{min}}, \quad i_o = -\frac{d_{min}}{d_{max} - d_{min}}. \tag{18}$$

Strategy II. ON–OFF: The simplified ON–OFF strategy uses a single ON–OFF activation surface (ellipse characterized by d_o and v_o); the maximum current is turned on when the instantaneous vector magnitude is outside the ON–OFF activation surface and turned off when inside this surface. A schematic explanation of the proposed linear current variation and ON–OFF strategies is presented in Figure 7.

Most motions with scale factors as defined in Table 1 can be accommodated without activating the BLS-CMRD in semi-active mode, as illustrated in Figure 6. Thus, the following analyses have been conducted with the suite of motions scaled up by a factor of 3 (300% of design level) to evaluate the control strategy as added protection for very rare motions that exceed the design level. The histories of vertical displacement and current at the left device are presented in Figure 8 for 300% of Manjil, Iran 1990–Abbar (ground motion #4) for (a) Passive-OFF (no current applied in the analysis); (b) linear current variation with $d_{min} = 12.5$ mm, $d_{max} = 22.5$ mm, and $d/v = 0.07$; and (c) ON–OFF control with $d_o = 17.5$ mm and $d/v = 0.07$. These histories show that the current is activated intermittently throughout the history according to the assigned thresholds in either control strategy. For linear current variation, the current intensity varies after passing the MR activation surface, and the upper bound current of 1 Amp associated with reaching the MR

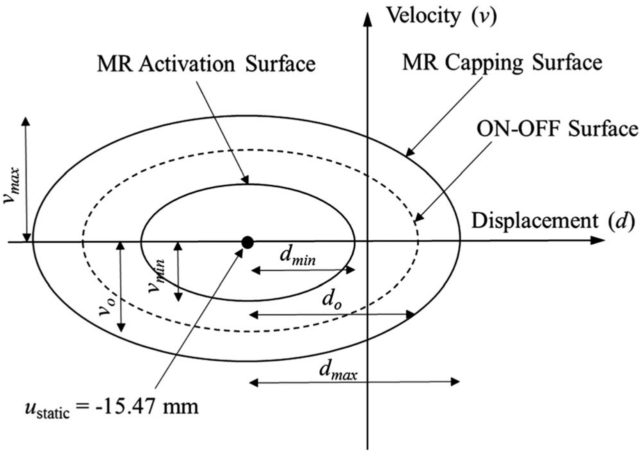

FIGURE 7 Proposed linear current variation and ON–OFF theory

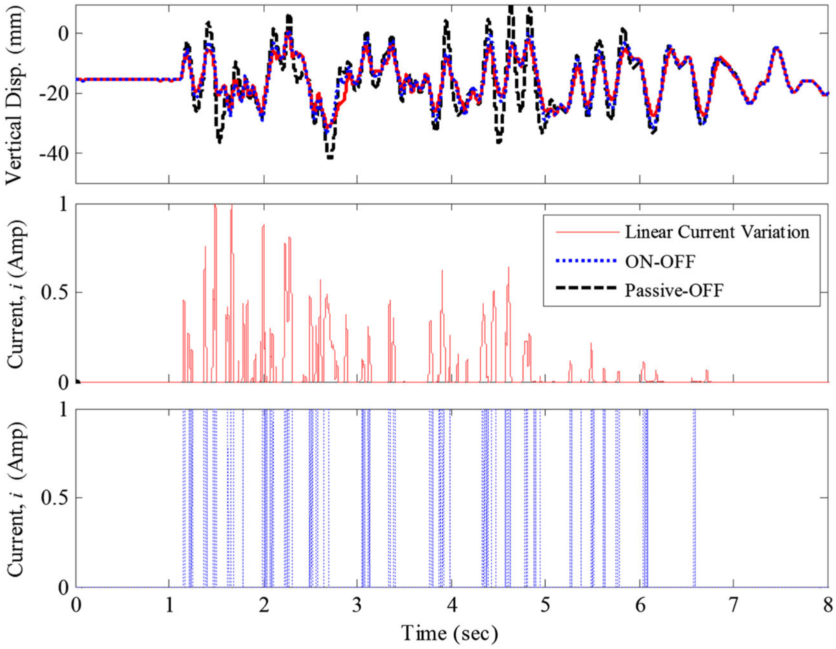

FIGURE 8 Vertical displacement and current history at left BLS-CMRD for Manjil, Iran 1990–Abbar

capping surface is rarely observed. However, for ON–OFF control, the current fluctuates instantaneously between 0 and 1 Amp at the threshold ON–OFF activation surface, with no variation in between. With the additional damping, substantial reduction in the vertical displacement at corresponding instances of current activation is achieved in both cases relative to Passive-OFF.

7 | PARAMETER SELECTION FOR LINEAR CURRENT VARIATION CONTROL

Next, a sensitivity study is presented, the results of which are used to select suitable activation and capping surface intensities for the proposed linear current variation strategy. In this study, the displacement and velocity limits were systematically varied. Several responses were considered to evaluate the control strategy, including those previously defined (peak vertical displacement and acceleration of the left BLS-CMRD, overall drift ratio), and two additional parameters, which are operation time and energy ratio for the controller. The operation time T_{op} represents the cumulative time that the current is activated, whereas the energy ratio E_r is calculated as follows:

$$E_r = \frac{E}{E_{passive-on}}, \tag{19}$$

$$E = \int_0^{T_{op}} i^2 r_i \, dt, \tag{20}$$

where E = energy and r_i = resistance. Equation (20) was derived from energy $E = \int_0^{T_{op}} p \, dt$ where p = power, $p = iv_t$ where v_t = voltage, and $v_t = ir_i$. T_{op} and E_r reflect the ability of the proposed linear current variation to control vertical isolator displacement without operating at full energy capacity. The maximum current is only activated when the combined displacement and velocity magnitude reaches the MR capping surface (determined by d_{max} and v_{max}) as shown previously in Figure 7.

For the sensitivity study, the following parameter variations were considered. First, d_{min} was varied from 10 to 20 mm with an increment of 2.5 mm, whereas d_{max} was kept constant at 22.5 mm. Second, d_{max} was varied from 12.5 to 22.5 mm with an increment of 2.5 mm, whereas d_{min} was kept constant at 10 mm. The d/v ratio was varied from 0.04 to 0.07 with an increment of 0.01 in both cases. Peak responses were computed for various combinations of d/v and d_{min} or d_{max}. Also, Passive-OFF and Passive-ON were considered for reference.

The median (over the 12 ground motions) of the peak absolute positive and negative vertical displacements, peak vertical acceleration, operation time T_{op} and energy ratio E_r for the left BLS-CMRD, as well as overall drift ratio, are presented as a function of d_{min} and d_{max} in Figures 9 and 10, respectively. Vertical displacement, drift ratio and vertical acceleration increase with increasing d_{min} as shown in Figure 9a,b,c. However, for increasing d_{max}, vertical displacement and drift ratio increase whereas vertical acceleration decreases as shown in Figure 10a,b,c. The increase in the peak positive and negative vertical displacement for increasing d_{min} is relatively small. As expected, peak absolute values of vertical displacement and drift ratio for linear current variation are bounded by Passive-OFF and Passive-ON cases. However, linear current variation helps reduce the vertical acceleration relative to both Passive-OFF and Passive-ON as desired for base isolation. Also, all studied cases mitigate the vertical acceleration below PGA, which is shown for reference in Figure 9c. The maximum permitted story drift ratio of 1.5% for design of isolated buildings[22] is shown for reference in Figures 9b and 10b. When varying d_{max}, drift ratio ≤ 1.5% for all d/v values, because of the low value selected for d_{min} (10 mm). However, when varying $d_{min,}$ drift ratio ≤ 1.5% only for d_{min} ≤ 13 mm and d/v = 0.06 or 0.07.

linear current variation leads to great reductions in operation time and consumed energy relative to Passive-ON as it is designed to scale the current relative to the instantaneous magnitude of response rather than apply the maximum current continuously. Note the reference median operation time T_{op} = 22.5 s for Passive-ON. Operation time decreases as d_{min} increases (Figure 9d) but is almost unaffected by changes in d_{max} (Figure 10d), because d_{max} only affects the amount of current applied. With regard to energy usage, increasing d_{min} increases the magnitude of the activation surface, thus reducing the contribution of MR damping (reducing E_r; Figure 9e). On the other hand, increasing d_{max} increases the magnitude of the capping surface that activates the full current, thus decreasing the contribution of MR damping (Figure 10e). In general, E_r is higher when d_{min} is set to 10 mm and d_{max} is varied, than when d_{max} is set to

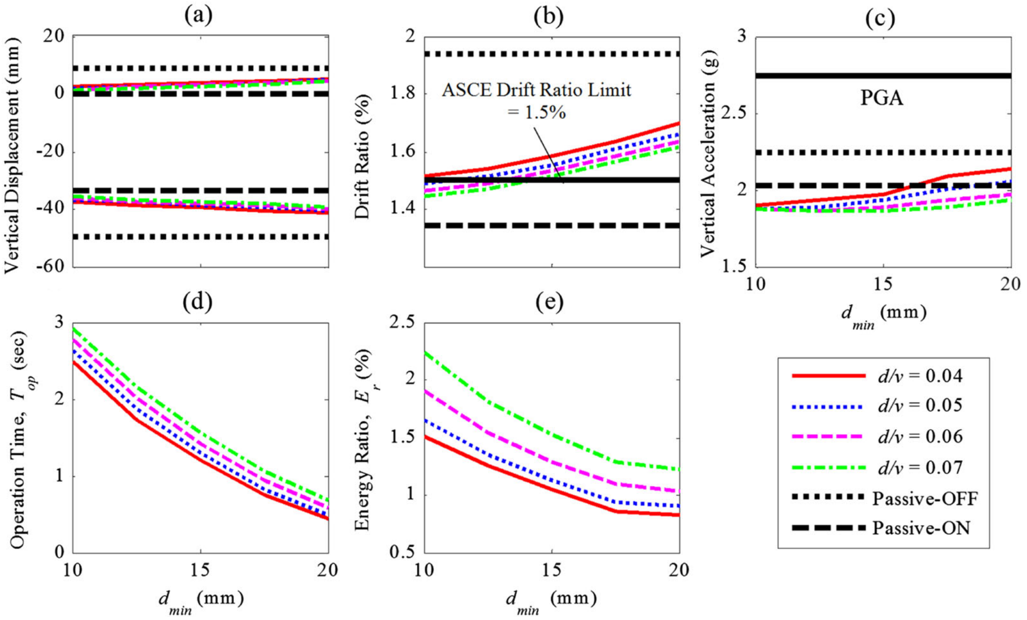

FIGURE 9 Median of peak responses at left BLS-CMRD for dmin = 10–20 mm, dmax = 22.5 mm and *d/v*, (a) vertical displacement, (b) drift ratio, (c) vertical acceleration, (d) operation time, (e) energy ratio

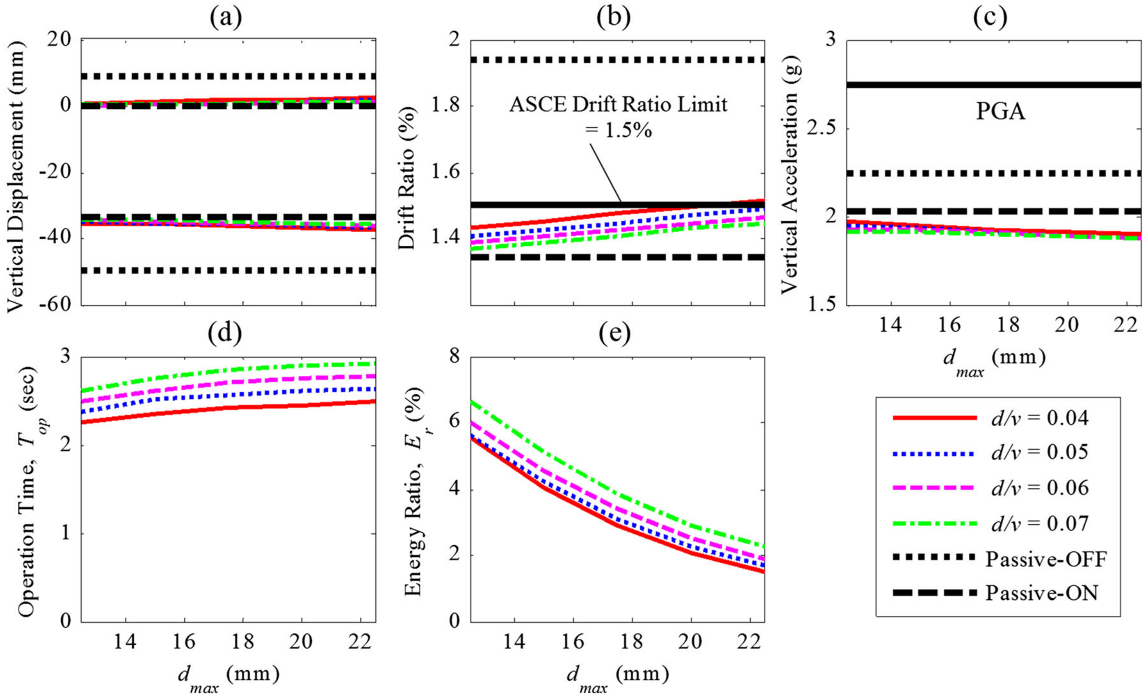

FIGURE 10 Median of peak responses at left BLS-CMRD for dmax = 12.5–22.5 mm, dmin = 10 mm and *d/v*, (a) vertical displacement, (b) drift ratio, (c) vertical acceleration, (d) operation time, (e) energy ratio

22.5 mm and d_{min} is varied. However, the efficiency of linear current variation is shown for all cases of d_{min} and d_{max} because $E_r < 10\%$.

The drift limit is the governing consideration for optimization of the proposed control strategy parameters. Optimized parameters are selected to be $d_{min} = 12.5$ mm, $d_{max} = 22.5$ mm, and $d/v = 0.07$. The selected parameters keep the median drift ratio below the ASCE limit, limit the device operation time, and keep the energy ratio < 2.0% for the examined 300% of design level intensity. However, it can be shown that this proposed control strategy gives very similar results to Passive-OFF case for design level motions. Likewise, optimized ON–OFF surface parameters are selected to be $d_o = 17.5$ mm and $d/v = 0.07$, which represents an ON–OFF activation surface that is midway between (or an average of) the MR activation and MR capping surfaces according to optimization analysis.

8 | DISP/VEL BASED CONTROL COMPARED WITH A BENCHMARK CONTROL STRATEGY

The clipped optimal control approach proposed by Dyke is a well known and effective algorithm that has been used with MR dampers.[20,21] The approach creates a force feedback loop that approximately computes a desired force f_d (optimal control force) in the control device:

$$f_d = \mathcal{L}^{-1}\left\{-\mathbf{K}_c(s)\mathcal{L}\left(\begin{bmatrix} y \\ f_{mr}+f_f \end{bmatrix}\right)\right\}, \tag{21}$$

where $\mathcal{L}\{.\}$ is the Laplace transform, and $\mathbf{K}_c(s)$ is linear controller designed to compute f_d based on the instantaneous measured responses y and measured force $f_{mr} + f_f$ in the device. The controller $\mathbf{K}_c(s)$ can be obtained from variety of synthesis methods. The force f_d is generated by controlling the applied current i as follows:

$$i = i_{\max}\,\mathrm{H}\left\{\left(f_d - f_{mr} + f_f\right)\left(f_{mr} + f_f\right)\right\}, \tag{22}$$

where $i_{\max}$ is the maximum applied current—1 Amp in this study—and H (.) is the Heaviside step function. The clipped optimal approach implements the simple strategy that if the desired force f_d is greater than the measured force, the maximum current is turned on; otherwise, the current is turned off.

The proposed linear current variation and ON–OFF control strategy are compared with the clipped optimal approach, by analyzing the system subjected to the suite of 12 ground motions scaled to 300% of design intensity, with the various control strategies applied. Peak positive and negative vertical displacements (relative to the static displacement), peak vertical acceleration, and overall peak drift ratio, for all cases at the left BLS-CMRD, are presented in Figure 11. Peak responses are presented for each individual excitation; also shown are the median, 84th percentile and 16th percentile over the suite of 12 motions.

The three control strategies (linear current variation, ON–OFF strategy, and clipped optimal) all lead to peak drift ratio and relative negative and positive vertical displacements that are reduced relative to Passive-OFF but increased relative to Passive-ON as illustrated in Figure 11a,b,c, respectively. Recall that relative positive vertical displacement $\leq |u_{\text{static}}| = 15.47$ mm means that no tension is sustained by the BLS-CMRD. The control strategies are generally not effective to prevent tension on average; however, the increased tension stiffness in the BLS-CMRD device ($k_t \approx 4k_c$) is effective to prevent very large tensile displacements from developing, especially with linear current variation and ON–OFF control. This leads to peak relative positive displacements that on average are considerably less than peak relative negative displacements (Figure 11a,b). Median drift ratio for proposed linear current variation and ON–OFF control strategy are achieving ASCE limit 1.5% and lower than clipped optimal approach. Average vertical accelerations for Passive-ON, linear current variation, and ON–OFF control are all lower than for Passive-OFF, whereas the average value for clipped optimal exceeds that for Passive-OFF. Importantly, the dispersion is higher for Passive-OFF confirming that the control strategies make the response more predictable. However, in all cases, peak vertical acceleration is lower than PGA, which shows that acceleration is attenuated (Figure 11c). In summary, the median, 16th and 84th percentiles for linear current variation, and ON–OFF strategy for all responses are very similar in value (indicating low dispersion) and have relatively lower response intensities than those for the clipped optimal approach.

Also, peak operation time T_{op} at the left BLS-CMRD for all cases with current applied as well as energy ratio E_r for all control cases are presented in Figure 12. Applying any control strategy leads to substantially reduced operation time compared with Passive-ON as presented in Figure 12a. For linear current variation, ON–OFF strategy, and clipped optimal, median $T_{op} = 2$, 0.8 and 1 s, respectively, whereas $T_{op} = 22.5$ s for Passive-ON. Linear current variation uses the least energy because it does not have to apply maximum current all the time as shown in Figure 12b. To better illustrate the application of current in different control strategies, the time history of current is presented for 300% of Loma Prieta, 1989–LGPC (ground motion #3) in Figure 13. For this motion, energy ratio $E_r = 1.3\%$, 2.5%, and 3.4% for linear current variation, ON–OFF strategy and clipped optimal approach, respectively, whereas T_{op} is 1.55, 0.6 and 0.75 s. The energy

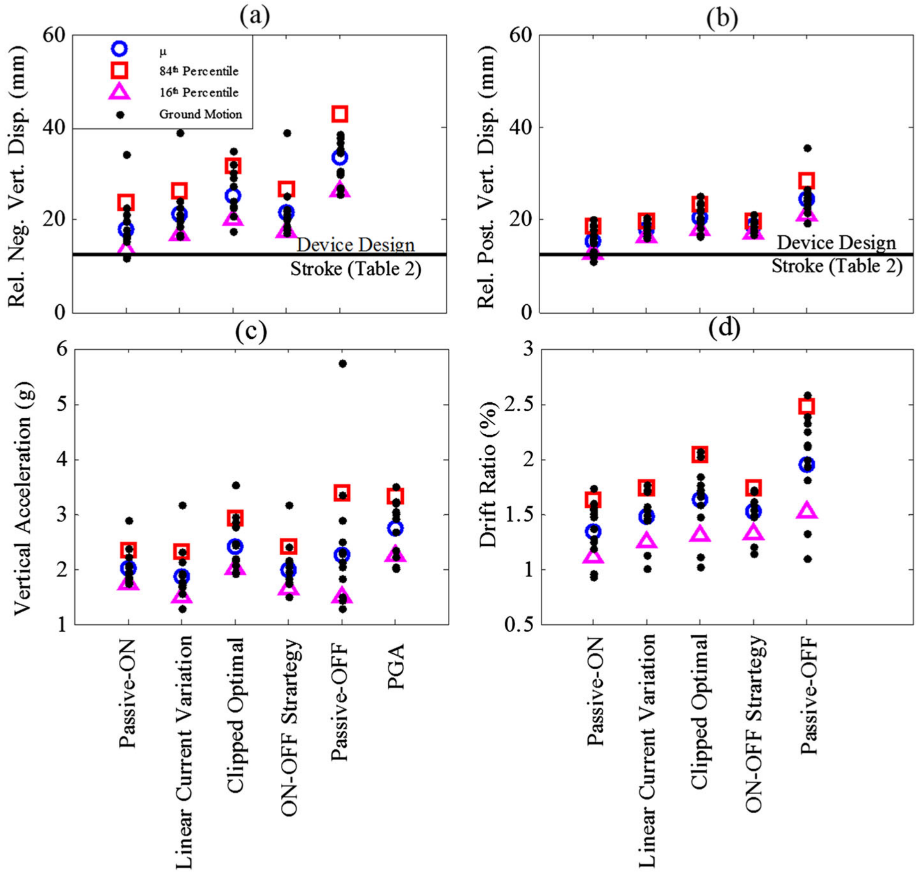

FIGURE 11 Peak responses at left BLS-CMRD, (a) relative negative vertical displacement, (b) relative positive vertical displacement, (c) vertical acceleration, (d) drift ratio

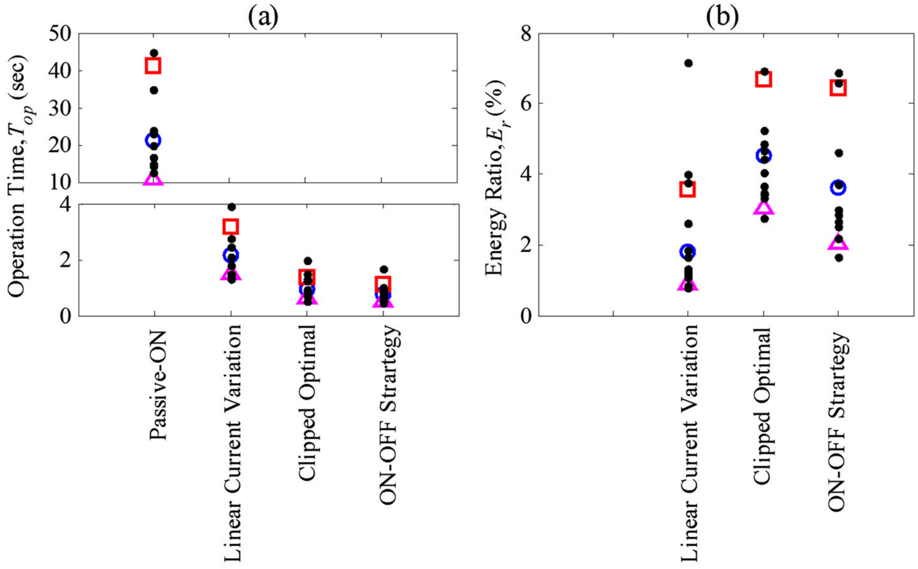

FIGURE 12 Peak responses at left BLS-CMRD, (a) operation time, (b) energy ratio

ratio is decreased while operating time is increased for linear current variation relative to the other two strategies. This is because the current is activated at smaller response intensities, but its intensity is more limited. On the other hand, clipped optimal operating time is higher than ON–OFF, but it does not lead to improved response control.

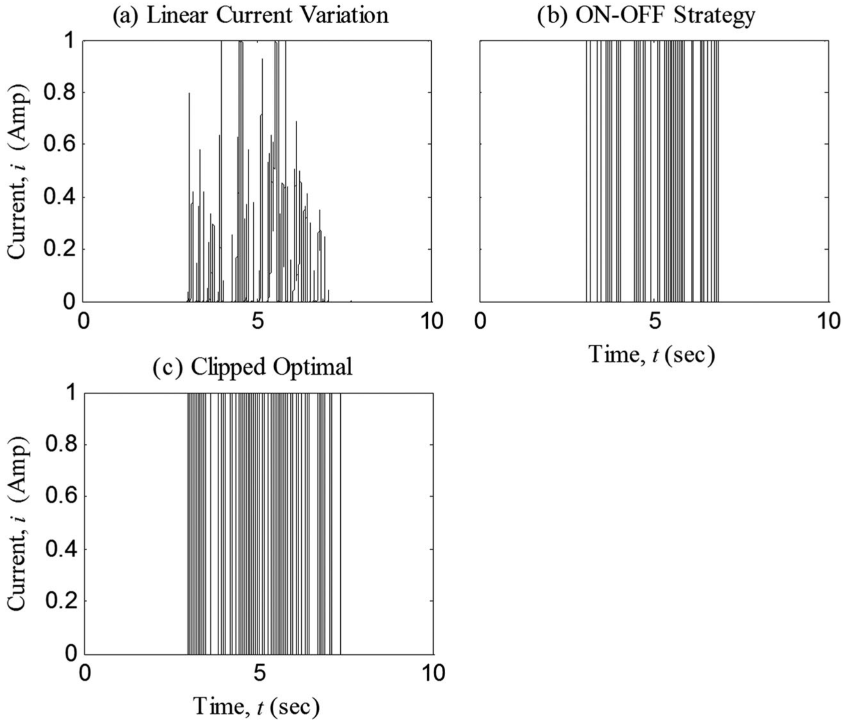

FIGURE 13 Current time history results for 300% of Loma Prieta, 1989–LGPC

9 | CONCLUSIONS

A simplified 2D rigid block supported on isolation bearings at the block edges was used to model a hypothetical building structure with both horizontal and vertical isolation. The isolation system was modeled as a combination of elastomeric bearings to resist horizontal shaking in series with BLS-CMRDs to resist vertical shaking. Elastomeric bearings were simulated with linear stiffness and damping, whereas BLS-CMRDs were simulated through a combination of nonlinear stiffness, and viscous and hysteretic (semi-active) damping. A Disp/Vel-based control strategy was proposed that adjusts the input current energy dissipation according to the instantaneous combined feedback displacement velocity of the damper device and aims to limit the displacement or stroke of the BLS-CMRD below its capacity. Two variations of the control strategy were explored. For linear current variation, the current is activated when a threshold lower bound magnitude of the vector combination of displacement and velocity is reached, and maximum current is applied when a threshold upper bound magnitude is reached. These threshold magnitudes are modeled as ellipse surfaces with displacement as the semi-major axis and velocity as the semi-minor axis; d_{min} and v_{min} are the magnitudes of displacement and velocity for the inner ellipse or MR activation surface, whereas d_{max} and v_{max} are magnitudes of displacement and velocity for the outer ellipse, denoted the MR capping surface. Alternatively, the simplified ON–OFF strategy uses a single ON–OFF activation surface that triggers the maximum current to turn on when the instantaneous vector magnitude moves outside the surface and turn off when it moves back inside this surface. A parameter study was conducted to select the activation and capping surface intensities for the linear current variation strategy. The proposed linear current variation and ON–OFF control strategies were evaluated with reference to the well-known clipped optimal approach, Passive-ON and Passive-OFF.

This study has led to the following conclusions:

- When subjected to the ground motion suite representing design level shaking, Passive-ON reduced the BLS-CMRD vertical displacement and the overall drift ratio relative to Passive-OFF, but with a big penalty to acceleration, leading vertical acceleration demands to exceed the peak ground acceleration (PGA), which does not meet the objective of the isolation system. This indicated the need for a control strategy to moderate the level of energy dissipation.
- The proposed Displ/Vel-based control was designed to activate additional damping and control BLS-CMRD displacements for very rare ground motions that exceeded the design level. For the system subjected to the ground motion suite scaled to 300% of design level shaking, the control strategy was shown to moderate the level of energy dissipation, keep the device vertical displacement within the design stroke limit, and attenuate vertical acceleration below PGA.

- The control activation and capping surface parameters for the proposed linear current variation strategy were selected using a parameter variation study, with the objective that the system response satisfy the ASCE 7-16 drift limit for isolated buildings for a wide range of ground motion intensities.
- Both variations of Disp/Vel-based control (linear current variation and ON–OFF) reduced peak vertical acceleration, drift ratio, absolute negative, and positive device stroke responses relative to the well-known clipped optimal control.
- According to the analytical analysis, applying any control strategy substantially reduced the operation time compared with Passive-ON. For linear current variation, ON–OFF strategy, and clipped optimal; median $T_{op} = 2$, 0.8 and 1 s, respectively, whereas median $T_{op} = 22.5$ s for Passive-ON.
- According to the analytical analysis, Disp/Vel-based control greatly reduced the energy requirements relative to Passive-ON, as the energy ratio (fraction of energy used relative to Passive-ON) < 10% for all variations of the MR activation and capping surface, and under application of motion intensity up to 300% design level. As the energy ratio calculations depend on the intensity of the applied current, linear current variation used the least energy because the maximum current is not always applied.

ACKNOWLEDGEMENTS

This material is based upon work supported by the National Science Foundation under Grant CMMI 1437003. Any opinions, findings, conclusions, or recommendations expressed in this publication are those of the authors and do not necessarily reflect the views of National Science Foundation.

ORCID

Walaa Eltahawy https://orcid.org/0000-0001-5006-0894
Keri Ryan https://orcid.org/0000-0002-0076-1630

REFERENCES

1. Furukawa S, Sato E, Shi Y, Becker T, Nakashima M. Full-scale shaking table test of a base-isolated medical facility subjected to vertical motions. *Earthq Eng Struct Dyn*. 2013;42(13):1931-1949.
2. Ryan KL, Soroushian S, Maragakis E, Sato E, Sasaki T, Okazaki T. Seismic simulation of an integrated ceiling-partition wall-piping system at E-Defense. I: Three-dimensional structural response and base isolation. *J Struct Eng*. 2016;142(2):04015130.
3. Inoue K, Fushimi M, Moro S, Morishita M, Kitamura S, Fujita T. *Development of Three-Dimensional Seismic Isolation System for Next Generation Nuclear Power Plant. Paper presented at: 13th World Conference on Earthquake*. Canada: Vancouver, B.C; 2004.
4. Suhara J, Tamura T, Ohta K, Okada Y, Moro S. Research on 3-D base isolation system applied to new power reactor 3-D seismic isolation device with rolling seal type air spring: Part 1. Paper presented at: Transactions of the 17th International Conference on Structural Mechanics in Reactor Technology (SMiRT 17), 2003; Prague, Czech Republic.
5. Suhara J, Matsumoto R, Oguri S, Okada Y, Inoue K, Takahashi. Research on 3-D base isolation system applied to new power reactor 3-D seismic isolation device with rolling seal type air spring: Part 2. Paper presented at: 18th International Conference on Structural Mechanics in Reactor Technology, 2005; Beijing, China.
6. Kashiwazaki A, Shimada T, Fujiwaka T, Moro S. Study on 3-dimensional base isolation system applying to new type power plant reactor (hydraulic 3-dimensional base isolation system: No.1). Paper presented at: Transaction of the 17th International Conference on Structural Mechanics in Reactor Technology, 2003; Prague, Czech Republic.
7. Kageyama M, Iba T, Umeki K, Somaki T, Moro S. Development of three-dimensional base isolation system with cable reinforcing air spring. Paper presented at: Transaction of the 17th International Conference on Structural Mechanics in Reactor Technology, 2003; Prague, Czech Republic.
8. Kageyama M, Iba T, Umeki K, Somaki T, Hino Y, Moro S, Ikutama S. Study on three-dimensional seismic isolation system for next generation nuclear power plant: independent cable reinforced rolling-seal air spring. Paper presented at: 13th World Conference on Earthquake Engineering, 2004; Vancouver, B.C., Canada.
9. Zhou Z, Wong J, Mahin S. Potentiality of using vertical and three-dimensional isolation systems in nuclear structures. *Nucl Eng Technol*. 2016;48(5):1237-1251.
10. Eltahawy W, Ryan K, Cesmeci S, Gordaninejad F. Parameters affecting dynamic properties for 3-dimensional seismic isolation. *Submitted in*. *J Earthq Eng*.
11. Cesmeci S, Gordaninejad F, Ryan K, Eltahawy W. A liquid spring–magnetorheological damper system under combined axial and shear loading for three-dimensional seismic isolation of structures. *J Intell Mater Syst Struct*. 2018;29(18):3517-3532.

12. Dyke SJ, Spencer Jr BF. Seismic response control using multiple MR dampers. Paper presented at: Proc., 2nd Int. Workshop on Struc. Control, 1996; Hong Kong.
13. Gordaninejad F, Saiidi M, Hansen BC, Chang FK. Magnetorheological fluid dampers for control of bridges. Paper presented at: Proc., 2nd World Conf. on Struct. Control, 1999; Wiley, West Sussex, U.K.
14. Spencer DF, Dyke SJ, Sain MK, PhCarlson JD. Phenomenological model of a magnetor-heological damper. *J Eng Mech*. 1997;130(3):230-238.
15. Yoshida O, Dyke SJ. Response control of full-scale irregular buildings using magnetorheological dampers. *J Struct Eng*. 2005;131(5):734-742.
16. Rahbari NM, Azar BF, Talatahari S, Safari H. Semi-active direct control method for seismic aleviation of structures using MR dampers. *J Struct Contr Health Monit*. 2012;20(6):1021-1042.
17. Dyke SJ, Spencer Jr BF. A comparison of semi-active control strategies for the MR damper. Paper presented at: Proc., IASTED Intl. Conf. on Intelligent Information Sys., 1997; Los Alamitos, Calif.
18. Leitmann G. Semiactive control for vibration attenuation. *J Intell Mater Syst Struct*. 1994;5(6):841-846.
19. McClamroch NH, Gavin HP. Closed Loop Structural Control Using Electrorheological Dampers. Paper presented at: Proc. Am. Control Conference, 1995; Washington, D.C.
20. Dyke SJ, Spencer BF Jr, Sain MK, Carlson JD. Modeling and control of magnetorheological dampers for seismic response reduction. *Smart Mater Struct*. 1996;5:565-575.
21. Pohoryles DA, Duffour P. Adaptive control of structures under dynamic excitation using magnetorheological dampers: an improved clipped-optimal control algorithm. *J Vib Control*. 2015;21(13):2569-2582.
22. American Society of Civil Engineers (ASCE). ASCE Standard–ASCE/SEI 7–16: Minimum design loads for buildings and other structures. Reston, VA. Reston, VA. 2016.
23. National Earthquake Hazards Reduction Program (NEHRP). Recommended Seismic Provisions for New Buildings and Other Structures. FEMA P-750 2009.
24. Chiou BSJ, Daragh R, Gregor N, Silva W. NGA project strong-motion database. *Earthq Spectra*. 2008;24(1):23-44.
25. Zohuri B. *Dimensional Analysis and Self-Similarity Methods for Engineers and Scientists*. Albuquerque; New Mexico: Springer International Publishing Switzerland; 2015.
26. Cesmeci S. A Fail-safe, Bi-Linear Liquid Spring, Controllable Magnetorheological Fluid Damper for a Three-dimensional Earthquake Isolation System: Unversity of Nevada, Reno; 2017.
27. Charalampakis AE, Koumousis VK. A Bouc–Wen model compatible with plasticity postulates. *J Sound Vib*. 2009;322:954-968.

How to cite this article: Eltahawy W, Ryan K, Cesmeci S, Gordaninejad F. Displacement/velocity-based control of a liquid spring—MR damper for vertical isolation. *Struct Control Health Monit*. 2019;26:e2363. https://doi.org/10.1002/stc.2363